Flutter analysis of highly flexible wings using higher-order 1D structural theories

Aerospace Science and Technology 180 (2027) 113746

Contents lists available at ScienceDirect

Aerospace Science and Technology

journal homepage: www.elsevier.com/locate/aescte

Original article

Flutter analysis of highly flexible wings using higher-order 1D structural theories

Zhuolin Ying [a,b], Rodolfo Azzara [c], Matteo Filippi [c], Ma Xiaoping [b], Marco Petrolo [c,*]

[a] Institute of Engineering Thermophysics, Chinese Academy of Sciences, Beijing, 100190, China
[b] School of Space Exploration, University of Chinese Academy of Sciences, Beijing, 100049, China
[c] MUL2 Lab, Department of Mechanical and Aerospace Engineering, Politecnico di Torino, Corso Duca degli Abruzzi 24, Torino, 10129, Italy

ARTICLE INFO

Communicated by Dr Jiaqing Kou

Keywords:
Structural theories
Aeroelasticity
Flutter
Geometric nonlinearity
High-aspect-ratio wings

ABSTRACT

This paper presents a computational framework for the aeroelastic analysis of highly flexible high-altitude wings. The structural model is formulated within the Carrera Unified Formulation (CUF), which incorporates lower- and higher-order beam models and uses both Taylor and Lagrange expansion functions for the cross-section kinematics. The Vortex Lattice Method (VLM) and Doublet Lattice Method (DLM) are adopted for aerodynamic loads, and the Infinite Plate Spline (IPS) technique is employed for mesh-to-mesh mapping. A key element of the approach is the piecewise linearization strategy for flutter analysis. Static aeroelastic equilibrium is first computed iteratively under specified flight conditions; the tangent stiffness matrix is then extracted at the equilibrium state, and modal analysis is performed. The p-k method determines the flutter boundary. Numerical investigations of a benchmark High-Altitude Long-Endurance (HALE) wing show that geometric nonlinearity significantly reduces the flutter speed. Furthermore, DLM aerodynamics predicts 10–15% higher flutter speeds than strip theory. The CUF-based predictions show good agreement with reference solutions from the literature, underscoring the proposed framework's capability to support preliminary aircraft design through fast, efficient aeroelastic analyses based on 1D finite elements.

1. Introduction

High-Altitude Long-Endurance (HALE) aircraft employ high-aspect-ratio wings made of lightweight composite materials to maximize aerodynamic efficiency [1,2]. The resulting structures exhibit pronounced flexibility, resulting in large static deflections under aerodynamic and gravitational loads. The geometric nonlinearities alter the structure's dynamic characteristics [2], and, consequently, traditional linear aeroelastic analysis methods may be inadequate for reliably predicting the flutter boundaries of such highly flexible wings.

The work of Patil et al. [1] investigated the nonlinear effects in the aeroelastic behavior of HALE wings and showed that large wing deflections can reduce flutter speed significantly. Similar results were reported by Tang and Dowell [3], who showed that static pre-flutter deformation changes structural stiffness and stability, and by Patil and Hodges [4], who examined the relative roles of structural and aerodynamic geometric nonlinearities in high-aspect-ratio wings. Their analyses showed that large static deflections modify the structural natural frequencies and mode shapes; consequently, aeroelastic stability should be evaluated about the deformed equilibrium rather than using the modal basis of the undeformed configuration. Subsequent studies have further enhanced the fidelity of both structural and aerodynamic modeling. On the structural side, the beam theory of Hodges [5] and the strain-based formulations developed by Cesnik et al. [6,7] have been widely adopted, while the SHARPy framework based on displacement-based geometrically exact beam theory was introduced by Palacios et al. [8]. Regarding aerodynamic modeling, work has progressed from 2D strip theories with Peters' finite-state inflow [9] to the Unsteady Vortex Lattice Method (UVLM) and the Doublet Lattice Method (DLM) [10]. The Pazy Wing benchmark case was introduced by Avin et al. [11], and the collaborative analyses within the Third Aeroelastic Prediction Workshop (AePW3) [12,13] have provided valuable experimental and computational data for validating nonlinear aeroelastic codes. Riso and Cesnik [14] provided systematic comparisons of modeling approaches, offering detailed assessments of low-order model fidelity for very flexible wings. Investigations by Cheng et al. [15] have further demonstrated the importance of capturing geometric nonlinearities across different aeroelastic phenomena, including gust response of flexible aircraft with novel wing configurations.

The focus of this paper is to improve the structural modeling of flexible wings using higher-order beam theories. Lower-order beam theories such as Euler–Bernoulli [16,17] and Timoshenko [18] fail to

* Corresponding author.
E-mail address: marco.petrolo@polito.it (M. Petrolo).

https://doi.org/10.1016/j.ast.2026.113746
Received 28 May 2026; Received in revised form 16 August 2026; Accepted 3 September 2026
Available online 6 September 2026
1270-9638/

capture non-classical effects, including cross-sectional warping, in-plane deformation, and bending-torsion coupling that become significant in thin-walled composite wing structures. While three-dimensional (3D) finite elements (FE) can provide accurate solutions, their computational cost remains prohibitive for iterative aeroelastic analyses and parametric design studies. The Carrera Unified Formulation (CUF) [19,20] provides a hierarchical structural modelling approach in which the order of the cross-sectional displacement expansion is a free parameter, enabling systematic refinement from classical beam theories to higher-order models that capture 3D stress distributions. The effectiveness of one-dimensional (1D) CUF models in reproducing 3D structural behaviour has been extensively validated for static [21], free-vibration [22], and composite applications [23]. The extension of CUF to aeroelastic problems was initiated by Varello et al. [24], who coupled CUF beam models with the VLM for static aeroelastic analysis. Subsequently, Petrolo [25,26] and Pagani et al. [27] developed CUF-based flutter analysis frameworks using the DLM, demonstrating the capability of refined 1D models to accurately predict flutter conditions for both isotropic and composite lifting surfaces. Recent reduced-order approaches include an aeroelastic beam finite element for time-domain preliminary analysis [28] and a refined aeroelastic beam finite element for the stability analysis of flexible wings [29]; nonlinear modeling and control of wing flutter have also been investigated [30]. Benedetti et al. [31,32] extended CUF to the discontinuous Galerkin method and CFD. Azzara et al. [33] employed 1D and 2D higher-order theories based on the CUF in combination with Computational Fluid Dynamics (CFD) to study the role of shear and cross-section deformability in the static aeroelastic response.

Previous CUF aeroelastic papers [25–27] adopted refined structural models for static aeroelasticity and flutter without the effect of the geometrical nonlinearity. The present work extends the CUF aeroelastic framework to incorporate geometric nonlinearity through a piecewise linearization strategy and to predict the flutter onset boundary based on linearized stability of equilibrium states. The methodology proceeds as follows: 1) the nonlinear static aeroelastic equilibrium is computed iteratively using CUF coupled with VLM under specified flight conditions; 2) the tangent stiffness matrix is extracted at each equilibrium state, and modal analysis is computed in each state; 3) DLM computes unsteady aerodynamic influence coefficients; 4) the p-k method is employed to determine the flutter boundary. The aero-structural coupling is realized via the Infinite Plate Spline (IPS) technique [34] and the consistency of the present formulation is further assessed against commercial software results and reference solutions available in the literature.

This paper is structured as follows: Section 2 presents the aeroelastic formulation, Section 3 describes the numerical model and results, and, finally, Section 4 summarizes the conclusions.

2. Aeroelastic formulation

2.1. Structural theories and finite elements

The structural model is formulated within the CUF framework, a hierarchical approach that permits systematic refinement of kinematic assumptions [19]. In 1D CUF, the 3D displacement field, $\boldsymbol{u}(x, y, z)$, is expressed as an expansion over the beam cross-section:

$$\boldsymbol{u}(x, y, z) = F_\tau(x, z)\boldsymbol{u}_\tau(y), \qquad \tau = 1, \dots, M \tag{1}$$

$F_\tau(x, z)$ are cross-sectional expansion functions, $\boldsymbol{u}_\tau(y)$ is the generalized displacement vector, M is the number of expansion terms, and the repeated subscript τ implies summation according to Einstein's notation. The choice of expansion functions F_τ is arbitrary in the CUF framework, enabling different classes of refined beam theories to be implemented within a unified formulation. Two expansion functions are considered: Taylor expansions (TE) using polynomial terms $x^i z^j$, and Lagrange expansions (LE) using Lagrange polynomials defined at discrete cross-sectional points. The present work employs the nine-node Lagrange polynomials (LE9) and TE terms up to fourth order. The LE9 polynomials in normalized coordinates $(\alpha, \beta) \in [-1, 1]^2$ are given by Carrera et al. [19]:

$$\begin{aligned} F_\tau &= \frac{1}{4}(\alpha^2 + \alpha\alpha_\tau)(\beta^2 + \beta\beta_\tau), \quad \tau = 1, 3, 5, 7 \\ F_\tau &= \frac{1}{2}\beta_\tau^2(\beta^2 + \beta\beta_\tau)(1 - \alpha^2) + \frac{1}{2}\alpha_\tau^2(\alpha^2 + \alpha\alpha_\tau)(1 - \beta^2), \quad \tau = 2, 4, 6, 8 \\ F_9 &= (1 - \alpha^2)(1 - \beta^2) \end{aligned} \tag{2}$$

$(\alpha_\tau, \beta_\tau)$ are the normalized coordinates of the LE9 nodes. Along the beam axis, the finite element method (FEM) is adopted:

$$\boldsymbol{u}_\tau(y) = N_i(y)\boldsymbol{q}_{\tau i}, \qquad i = 1, \dots, N_n \tag{3}$$

$N_i(y)$ are the shape functions, $\boldsymbol{q}_{\tau i}$ contains the nodal displacement vector, and N_n is the number of nodes per element. In this paper, classical 1D FE with four nodes (B4) employing a cubic approximation along the beam axis is used. Combining Eqs. (1) and (3), the complete displacement field becomes:

$$\boldsymbol{u}(x, y, z) = F_\tau(x, z)N_i(y)\boldsymbol{q}_{\tau i} \tag{4}$$

The strain field is obtained from the displacement through linear differential operators. Following Carrera et al. [19], the six-component strain vector is split into two groups according to their association with the cross-sectional plane and the beam axis:

$$\boldsymbol{\epsilon}_p = \{\epsilon_{xx},\ \epsilon_{zz},\ \gamma_{xz}\}^T, \qquad \boldsymbol{\epsilon}_n = \{\epsilon_{yy},\ \gamma_{xy},\ \gamma_{yz}\}^T \tag{5}$$

p denotes in-plane (cross-sectional) components and n denotes components involving the beam-axis direction y. The strain–displacement relations are:

$$\boldsymbol{\epsilon}_p = \boldsymbol{D}_p\,\boldsymbol{u}, \qquad \boldsymbol{\epsilon}_n = (\boldsymbol{D}_{n\Omega} + \boldsymbol{D}_{ny})\,\boldsymbol{u} \tag{6}$$

$$\boldsymbol{D}_p = \begin{bmatrix} \partial_x & 0 & 0 \\ 0 & 0 & \partial_z \\ \partial_z & 0 & \partial_x \end{bmatrix}, \quad \boldsymbol{D}_{n\Omega} = \begin{bmatrix} 0 & 0 & 0 \\ 0 & \partial_x & 0 \\ 0 & \partial_z & 0 \end{bmatrix}, \quad \boldsymbol{D}_{ny} = \begin{bmatrix} 0 & \partial_y & 0 \\ \partial_y & 0 & 0 \\ 0 & 0 & \partial_y \end{bmatrix} \tag{7}$$

$\boldsymbol{D}_p$ contains derivatives with respect to the cross-sectional coordinates (x, z), $\boldsymbol{D}_{n\Omega}$ collects cross-sectional derivatives appearing in the beam-axis strain components, and $\boldsymbol{D}_{ny}$ involves differentiation along the beam axis y. The stress–strain constitutive relation is similarly partitioned:

$$\begin{Bmatrix} \boldsymbol{\sigma}_p \\ \boldsymbol{\sigma}_n \end{Bmatrix} = \begin{bmatrix} \tilde{\boldsymbol{C}}_{pp} & \tilde{\boldsymbol{C}}_{pn} \\ \tilde{\boldsymbol{C}}_{np} & \tilde{\boldsymbol{C}}_{nn} \end{bmatrix} \begin{Bmatrix} \boldsymbol{\epsilon}_p \\ \boldsymbol{\epsilon}_n \end{Bmatrix} \tag{8}$$

$\tilde{\boldsymbol{C}}$ is the material stiffness matrix partitioned consistently with the strain decomposition. For orthotropic materials, the sub-matrices $\tilde{\boldsymbol{C}}_{pn}$ and $\tilde{\boldsymbol{C}}_{np}$ contain the coupling terms between in-plane and beam-axis stress/strain components. The governing equations are derived through the principle of virtual work:

$$\delta L_{int} = -\delta L_{ine} \tag{9}$$

$$\delta L_{int} = \int_V \delta\boldsymbol{\epsilon}^T\boldsymbol{\sigma}\,dV = \delta\boldsymbol{q}_{sj}^T\boldsymbol{K}^{ij\tau s}\boldsymbol{q}_{\tau i} \tag{10}$$

Substituting Eqs. (6)–(8) into the virtual work statement, and considering Eq. (4), the fundamental nucleus (FN) of the stiffness matrix is obtained as a 3×3 array [19,26]. The key property of CUF is that this formal expression remains unchanged regardless of the expansion order. Similarly, the mass matrix stems from:

$$\delta L_{ine} = \int_V \rho\delta\boldsymbol{u}^T\ddot{\boldsymbol{u}}\,dV = \delta\boldsymbol{q}_{sj}^T\boldsymbol{M}^{ij\tau s}\ddot{\boldsymbol{q}}_{\tau i} \tag{11}$$

ρ is the material density. The undamped free vibration problem is then formulated as:

$$(-\omega^2\boldsymbol{M} + \boldsymbol{K})\boldsymbol{\phi} = \boldsymbol{0} \tag{12}$$

ω is the natural circular frequency and $\boldsymbol{\phi}$ is the corresponding mode shape. For structures undergoing large displacements, the linear strain–displacement relations of Eq. (6) are augmented with higher-order

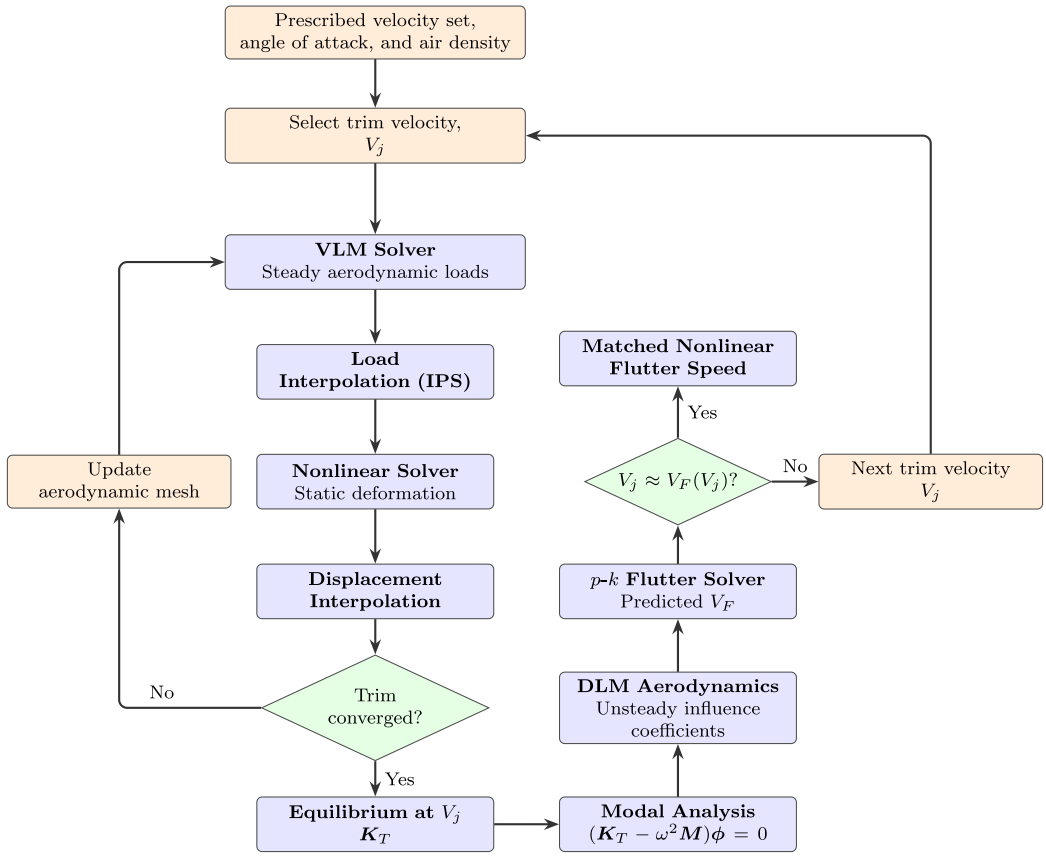

Fig. 1. Flowchart of the geometrically nonlinear flutter analysis. For each prescribed trim velocity, the static coupling is iterated to equilibrium, and the flutter speed is then evaluated using the tangent stiffness matrix.

terms through the Green–Lagrange strain tensor, see [27]. By linearizing about a known equilibrium state $\boldsymbol{u}_0$, the tangent stiffness matrix reads:

$$\boldsymbol{K}_T = \boldsymbol{K}_0 + \boldsymbol{K}_\sigma(\boldsymbol{u}_0) + \boldsymbol{K}_u(\boldsymbol{u}_0) \tag{13}$$

$\boldsymbol{K}_0$ is the linear stiffness matrix, $\boldsymbol{K}_\sigma$ is the geometric stiffness matrix, and $\boldsymbol{K}_u$ is the initial displacement stiffness matrix that accounts for the displacement-dependent contributions of the nonlinear strain to the elastic forces. While $\boldsymbol{K}_0$ is constant, both $\boldsymbol{K}_\sigma$ and $\boldsymbol{K}_u$ depend on the current deformation state and must be updated at each iteration. The nonlinear static solution is computed using a full Newton–Raphson method with load control [19,27]. At a converged equilibrium state, the modal analysis reads

$$\left(\boldsymbol{K}_T - \omega^2 \boldsymbol{M}\right)\boldsymbol{\phi} = \boldsymbol{0} \tag{14}$$

$\boldsymbol{K}_T$ is the tangent stiffness evaluated at the converged static equilibrium, and the columns of $\boldsymbol{\Phi}$ collect the corresponding eigenvectors $\boldsymbol{\phi}$. Eq. (14) contains structural terms only; its eigenvectors provide the modal basis for the subsequent aeroelastic analysis.

2.2. Aeroelastic model

Two complementary aerodynamic methods are employed: VLM for steady loads in the iterative nonlinear static aeroelastic analysis [24,35], and DLM for unsteady aerodynamics in flutter analysis [10,25,36,37]. The standard aerodynamic kernel functions and panel-influence expressions are not repeated here; details can be found in [35,36]. The Infinite Plate Spline (IPS) is used for mesh-to-mesh mapping as documented in [34]. The eigenvectors obtained from Eq. (14) are used as the structural modal basis. Their displacements are interpolated to the aerodynamic grid through IPS and used with the DLM to obtain the modal generalized aerodynamic force matrix $\boldsymbol{Q}_{hh} = \boldsymbol{Q}^R_{hh} + i\boldsymbol{Q}^I_{hh}$. The resulting p-k flutter equation is given by Hassig [38]

$$\left[\left(\frac{V}{b}\right)^2 p^2 \boldsymbol{M}_r + \boldsymbol{K}_{T,r} - q_\infty\left(\boldsymbol{Q}^R_{hh}(M_\infty, k) + \frac{p}{k}\boldsymbol{Q}^I_{hh}(M_\infty, k)\right)\right]\hat{\boldsymbol{\eta}} = \boldsymbol{0}, \tag{15}$$

where $\hat{\boldsymbol{\eta}}$ is the complex vector of modal amplitudes, $\boldsymbol{M}_r = \boldsymbol{\Phi}^T\boldsymbol{M}\boldsymbol{\Phi}$ and $\boldsymbol{K}_{T,r} = \boldsymbol{\Phi}^T\boldsymbol{K}_T\boldsymbol{\Phi}$ are the reduced mass and tangent stiffness matrices, and $q_\infty = \rho_\infty V^2/2$ is the dynamic pressure. The reference semi-chord is $b = c/2$. The nondimensional complex eigenvalue is $p = k(\gamma + i)$, where $k = \omega b/V$ is the reduced frequency, ω is the aeroelastic circular frequency, and $g = 2\gamma$ is the modal damping parameter shown in the V-g diagrams. At each velocity, the p-k iterations enforce $\mathrm{Im}(p) = k$, and flutter is identified when $g = 0$.

To solve the static aeroelastic problem, an iterative procedure is employed that couples the VLM aerodynamic solver and the structural solver via the IPS interpolation scheme. The same procedure is used for CUF results and Nastran; see Fig. 1. The iterative procedure is considered converged when the relative change in wing-tip displacement between successive iterations falls below a prescribed tolerance:

$$\frac{\|\boldsymbol{u}^{(n)}_{tip} - \boldsymbol{u}^{(n-1)}_{tip}\|}{\|\boldsymbol{u}^{(n)}_{tip}\|} < \varepsilon_{tol} \tag{16}$$

n denotes the iteration count and $\varepsilon_{tol} = 10^{-4}$ is adopted in the present work. The converged static solution provides the tangent stiffness $\boldsymbol{K}_T$ (Eq. (13)) that serves as the baseline for dynamic stability assessment.

The flutter analysis proceeds as follows: (i) prescribe a set of candidate trim velocities V_j for the selected root angle of attack; (ii) compute the nonlinear static equilibrium using the VLM-CUF coupling at each V_j; (iii) extract the tangent stiffness matrix $\boldsymbol{K}_T$ (Eq. (13)) and perform modal analysis (Eq. (14)); (iv) compute DLM unsteady aerodynamic coefficients; and (v) solve the p-k flutter equation to obtain V_F. The

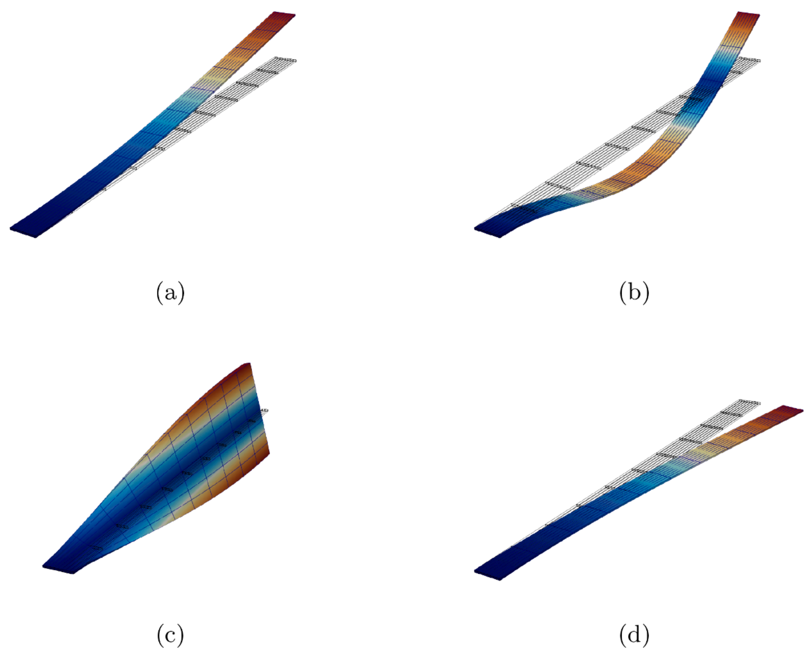

Fig. 2. First four natural modes of the undeformed HALE wing: (a) 1st bending, $f_1 = 0.357$ Hz; (b) 2nd bending, $f_2 = 2.236$ Hz; (c) 1st torsion, $f_3 = 4.968$ Hz; (d) in-plane bending, $f_4 = 5.006$ Hz. Gray mesh: undeformed configuration; colored surface: mode shape (For interpretation of the references to colour in this figure legend, the reader is referred to the web version of this article.).

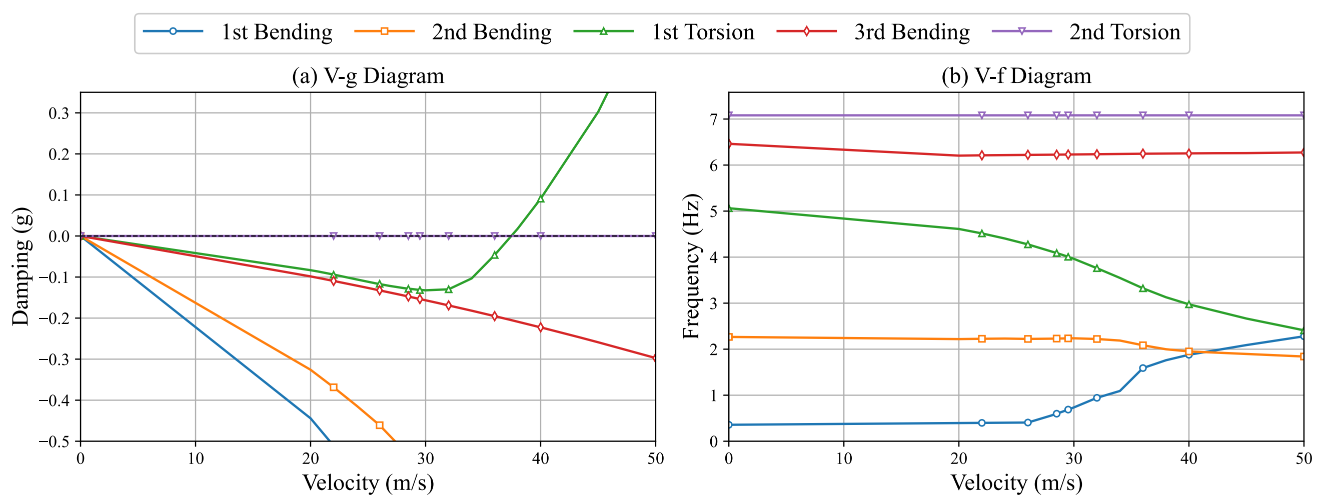

Fig. 3. V-g and V-f diagrams for linear flutter analysis using the 1D CUF model: (a) damping vs. velocity, (b) frequency vs. velocity. Flutter occurs at $V_F = 36.76$ m/s.

velocity-matching condition requires that the flight velocity at which static equilibrium is computed equals the predicted flutter speed. The geometrically nonlinear flutter speed is identified from the prescribed velocity sweep when:

$$\frac{|V_j - V_F(V_j)|}{V_F(V_j)} < \epsilon_{tol} \tag{17}$$

3. Results

The proposed aeroelastic framework is first verified using the HALE wing configuration, which has become a standard benchmark for nonlinear aeroelastic studies due to its pronounced flexibility and significant geometric nonlinear effects [1,6]. Assessments focus on mesh convergence, linear and nonlinear flutter analyses, and comparisons with literature reference data. Then, a wing with a NACA profile is considered.

3.1. HALE

The HALE wing properties follow those documented in [1,6]. The wing has a semi-span of 16 m and a constant chord of 1 m. The structural properties are representative of a highly flexible composite wing designed for sustained high-altitude flight. Table 1 summarizes the geometric, material, and atmospheric properties employed in the present analysis. The reference results are based on a clamped beam model whose inputs are the bending rigidity (EI), torsional rigidity (GJ), mass per unit length (m), and mass moment of inertia (I_α), without defining explicit cross-sectional geometry or material properties. To verify the current 1D CUF framework against this theoretical benchmark, an equivalent stiffness-matching strategy is adopted to define the cross-sectional properties of the 3D model. The wing cross-section is modeled as a rectangle with a chord $c = 1$ m and thickness $t = 0.0707$ m. The equivalent Young's modulus and shear modulus are back-calculated from the target

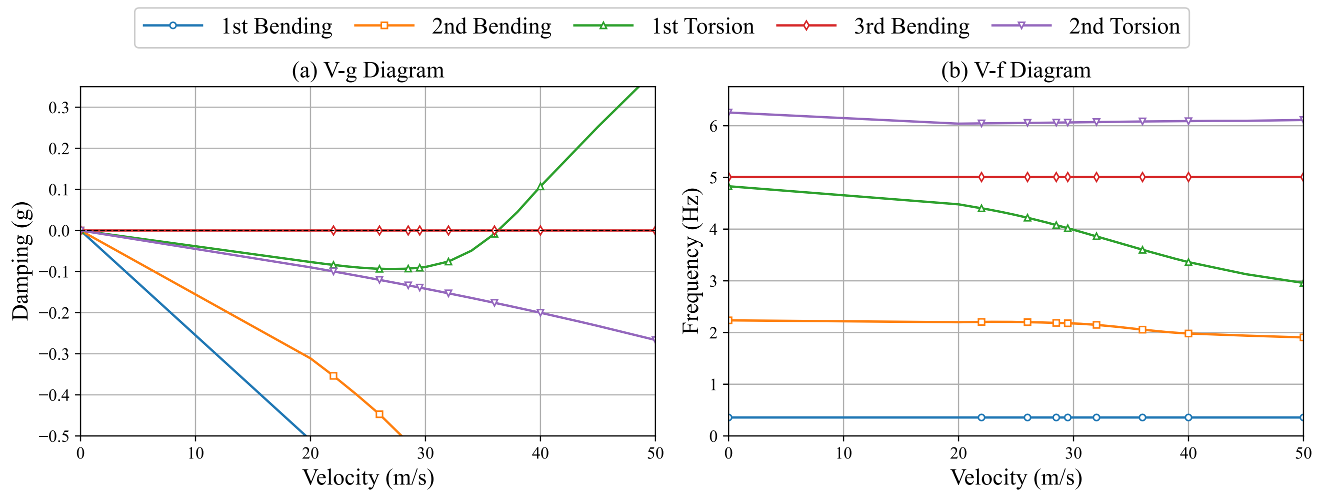

Fig. 4. V-g and V-f diagrams for linear flutter analysis using the MSC.Nastran shell model: (a) damping vs. velocity, (b) frequency vs. velocity. Flutter occurs at $V_F = 36.31$ m/s.

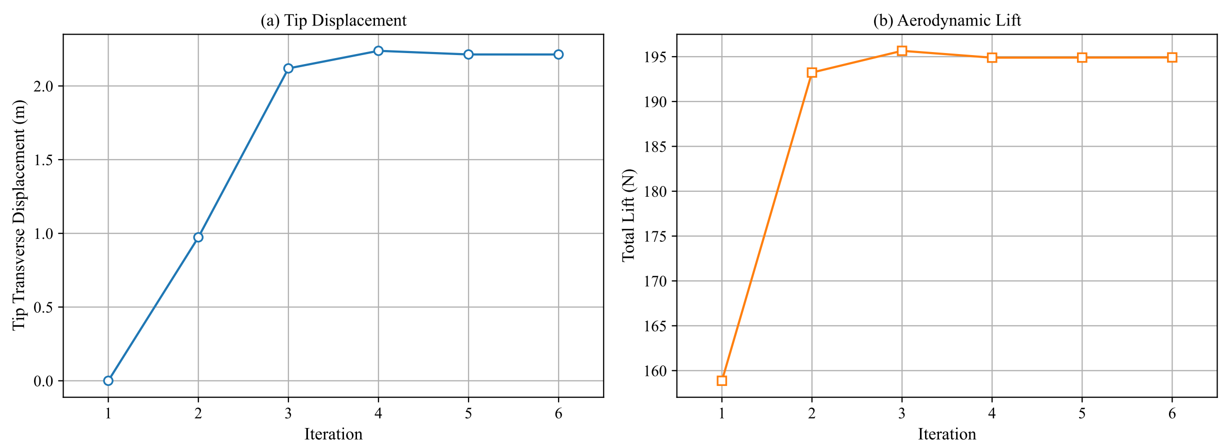

Fig. 5. Convergence history of VLM-CUF coupling: (a) tip displacement, (b) total lift; $V_\infty = 21.75$ m/s and $\alpha_0 = 5°$.

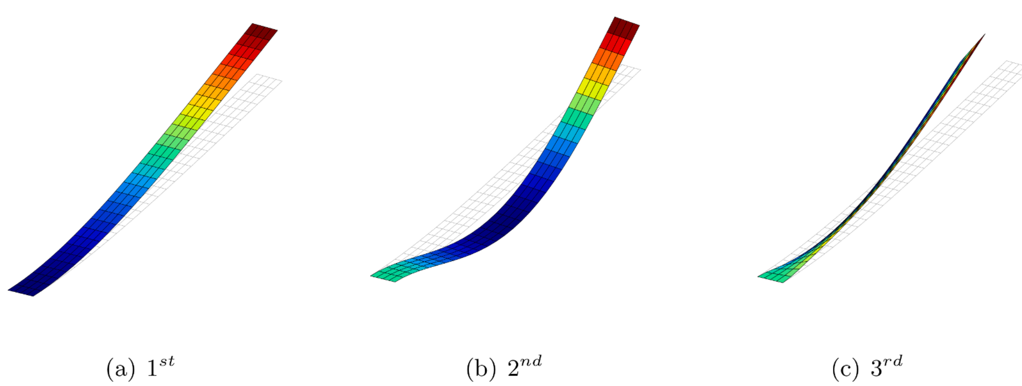

Fig. 6. First three modes at $V_\infty = 21.75$ m/s, $\alpha_0 = 5°$.

stiffness values:

$$E = \frac{12EI_z}{ct^3} = 6.788 \times 10^8 \text{ Pa}, \qquad G = \frac{3GJ}{ct^3} = 8.485 \times 10^7 \text{ Pa} \tag{18}$$

The material is modeled as orthotropic, with E and G independently specified rather than derived from isotropic relationships. This approach eliminates Poisson-coupling effects that would otherwise alter bending-torsion coupling. To simultaneously satisfy both the total mass per unit length ($m = 0.75$ kg/m) and the mass moment of inertia per unit length about the elastic axis ($I_\alpha = 0.1$ kg·m), a non-uniform density distribution is required. The cross-section is divided into three chordwise segments: leading edge (0–25% chord), central region (25–75% chord), and trailing edge (75–100% chord). The leading and trailing edge segments are assigned a density of $\rho_{LE/TE} = 19.092$ kg/m^3, while the central segment has $\rho_{center} = 2.1213$ kg/m^3. This distribution ensures the coincidence of the elastic axis and center of gravity at mid-chord and the mass and

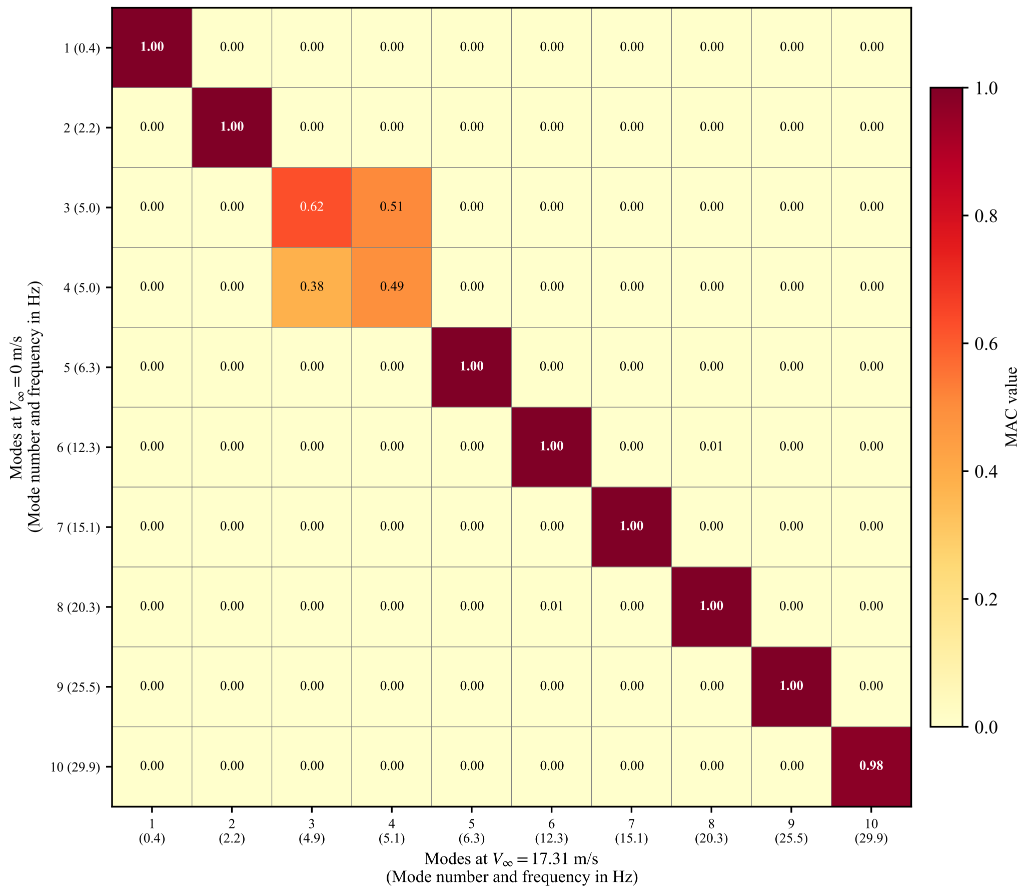

Fig. 7. MAC matrix comparing linear reference modes (rows) with modes at $V_\infty = 17.31$ m/s, $\alpha_0 = 5°$ (columns).

moment of inertia per unit length:

$$m = \int_A \rho \, dA = 0.75 \text{ kg/m}, \qquad I_\alpha = \int_A \rho (x - x_{EA})^2 \, dA = 0.1 \text{ kg} \cdot \text{m} \quad (19)$$

This modeling strategy is applied consistently to both the CUF beam model and the MSC.Nastran shell reference model, to avoid structural property mismatches. The aim of the shell model is to provide further verification. The wing is modeled as a flat plate with chord $c = 1$ m, span $L = 16$ m, and thickness $t = 0.0707$ m, using the orthotropic material properties from Eq. (18) and the non-uniform density distribution from Eq. (19). The shell model employs CQUAD8 elements (8-node quadrilaterals with quadratic interpolation).

3.1.1. Mesh convergence and structural theory assessment

A systematic convergence study is conducted to assess the sensitivity of the computed natural frequencies and flutter speeds to both structural mesh refinement and selection of the expansion order. Following the methodology adopted in [25], two distinct types of convergence are examined: (i) mesh convergence, where the number of FE is varied; (ii) cross-sectional model comparison, where TE and LE models of increasing order are compared to assess kinematic enrichment effects.

Table 2 presents the effects of mesh refinement on the natural frequencies, including the number of DOF. Based on these results, the 60×8 mesh is adopted for the MSC.Nastran reference model, providing converged results for all modes of interest. Concerning the CUF beam model, first, the influence of the spanwise mesh density is assessed by fixing the cross-sectional theory, i.e., 12LE9, and progressively increasing the number of B4 beam elements along the span. Table 3 reports the first four natural frequencies obtained with different spanwise discretizations. The effect of cross-sectional theories is then investigated by fixing the spanwise mesh, i.e., 20B4, and varying the number of LE9 elements over the cross-section, as shown in Table 4. The convergence study reveals that a 10B4-8LE9 model is as accurate as a 20B4-12LE9 model. Table 5 compares the natural frequencies obtained from different CUF kinematic theories. Both TE and LE models achieve excellent accuracy for global bending modes, with discrepancies below 0.5% compared to the reference. The torsional frequency shows greater sensitivity to kinematic theory selection: the TE2–TE4 models converge to approximately 5.02 Hz, while LE models converge to 4.97 Hz, with the MSC.Nastran shell model predicting 4.93 Hz. To systematically assess the influence of expansion type on aeroelastic predictions, a TE4 model is also employed for comparison throughout the subsequent linear flutter, nonlinear static aeroelastic, and nonlinear flutter analyses. The convergence study in Table 5 employs a 20B4 spanwise mesh for the TE models to ensure converged reference frequencies; however, for the subsequent aeroelastic analyses, a 10B4-TE4 configuration (1395 DOF) is adopted. This choice is motivated by the rapid convergence of TE models for global bending modes (Table 5) and the significant computational savings afforded by the lower DOF count, which is particularly advantageous for the iterative nonlinear trim procedure. Fig. 2 presents the first four natural modes of the converged HALE wing model. The first two modes are out-of-plane bending modes; the third is a torsional mode; and the fourth is an in-plane bending mode.

3.1.2. Linear flutter analysis

This section focuses on the convergence analysis of flutter. Table 6 presents the effects of spanwise structural mesh, cross-sectional theory, and aerodynamic panels on flutter speed and frequency. The results confirm that 10B4-8LE9 provides converged flutter and the MSC.Nastran

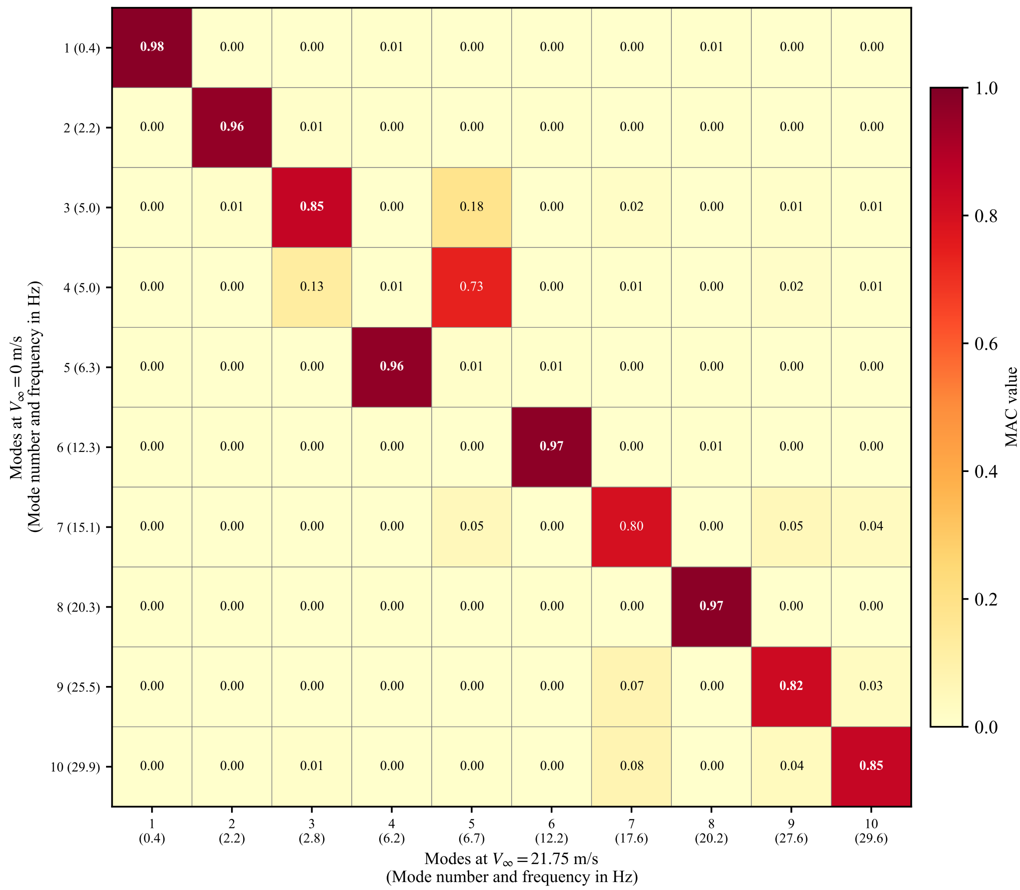

Fig. 8. MAC matrix comparing linear reference modes (rows) with modes at $V_\infty = 21.75$ m/s, $\alpha_0 = 5°$ (columns).

Table 1
HALE wing properties [1].

Property	Value	Unit
Geometric parameters		
Semi-span (L)	16	m
Chord (c)	1	m
Elastic axis location	50% chord	–
Center of gravity	50% chord	–
Structural properties		
Mass per unit length (m)	0.75	kg/m
Moment of inertia (50% chord)	0.1	kg·m
Bending rigidity (EI_z)	2×10^4	N·m^2
Torsional rigidity (GJ)	1×10^4	N·m^2
Chordwise bending rigidity (EI_x)	4×10^6	N·m^2
Flight conditions (altitude: 20 km)		
Air density (ρ_∞)	0.0889	kg/m^3

Table 2
Mesh convergence for the MSC.Nastran shell model natural frequencies (Hz).

Mesh	DOF	1^{st} Bend.	2^{nd} Bend.	1^{st} Tors.	1^{st} In-plane bend.
60×4	5094	0.357	2.235	4.929	5.007
60×8	9462	0.357	2.235	4.926	5.006
60×12	13,830	0.357	2.235	4.925	5.006

Table 3
Effect of spanwise beam elements on natural frequencies (Hz) with 12LE9 on the cross-section.

Mesh	DOF	1^{st} Bend.	2^{nd} Bend.	1^{st} Tors.	1^{st} In-plane bend.
5B4	3600	0.357	2.237	5.004	5.006
10B4	6975	0.357	2.236	4.974	5.006
15B4	10,350	0.357	2.236	4.969	5.006
20B4	13,725	0.357	2.236	4.968	5.006

Table 4
Effect of LE9 elements on natural frequencies (Hz) with 20B4 along the y-axis.

Mesh	DOF	1^{st} Bend.	2^{nd} Bend.	1^{st} Tors.	1^{st} In-plane bend.
4LE9	4941	0.357	2.236	5.004	5.006
8LE9	9333	0.357	2.236	4.978	5.006
12LE9	13,725	0.357	2.236	4.968	5.006

shell reference model shows excellent agreement (within 1.2%) with the converged CUF result. Together with the spanwise and modal comparisons in Tables 3 and 5, the 10B4-TE4 model predicts a flutter speed and frequency of 36.30 m/s and 3.68 Hz, compared with 36.31 m/s and 3.57 Hz from the MSC.Nastran shell model, while using 1395 rather than 9462 DOF. Thus, CUF provides a hierarchical means of retaining the structural modal characteristics relevant to flutter with a substantially smaller structural system. To systematically assess the influence of aerodynamic modeling fidelity, flutter analyses are performed using both 2D strip theory via MSC.Nastran's CAERO4/PAERO4 elements with Theodorsen aerodynamics and DLM. Table 7 provides a comparison of linear flutter predictions across different models. Figs. 3 and 4 present the V-g (velocity-damping) and V-f (velocity-frequency) diagrams from the flutter analyses for the CUF and MSC.Nastran structural models, respectively. The results show that:

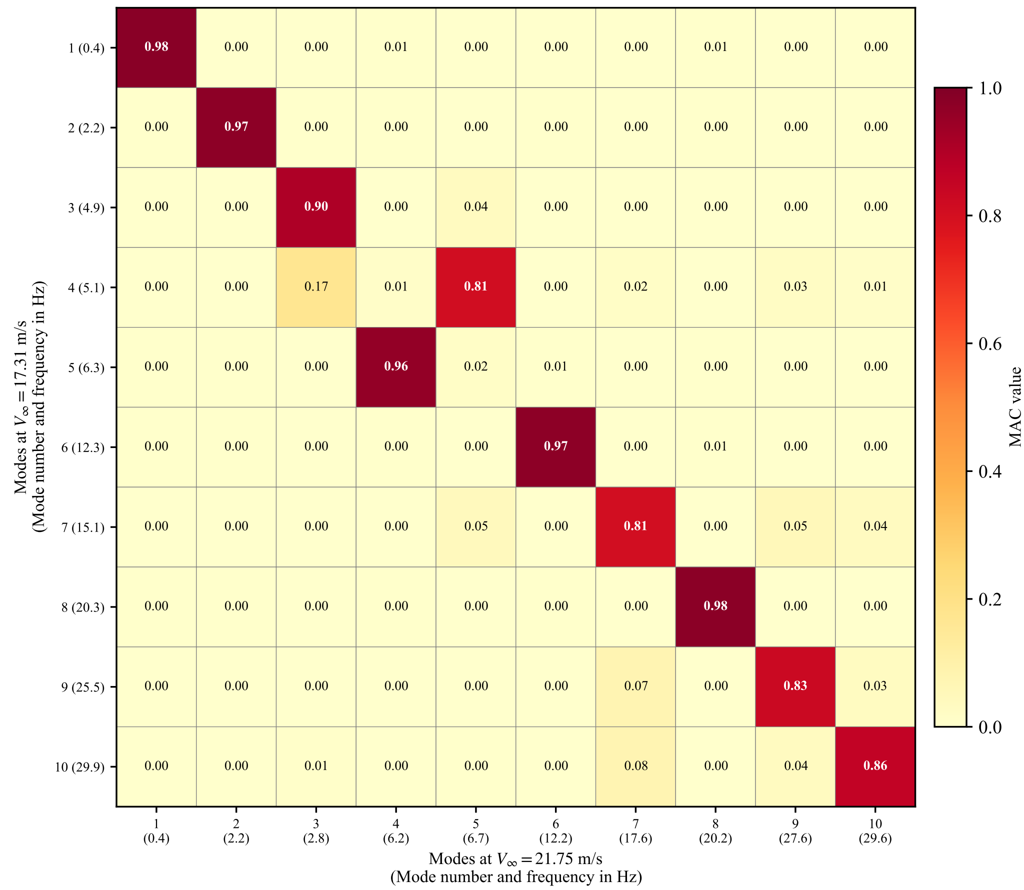

Fig. 9. MAC matrix comparing modes at $V_\infty = 17.31$ m/s (rows) with modes at $V_\infty = 21.75$ m/s (columns).

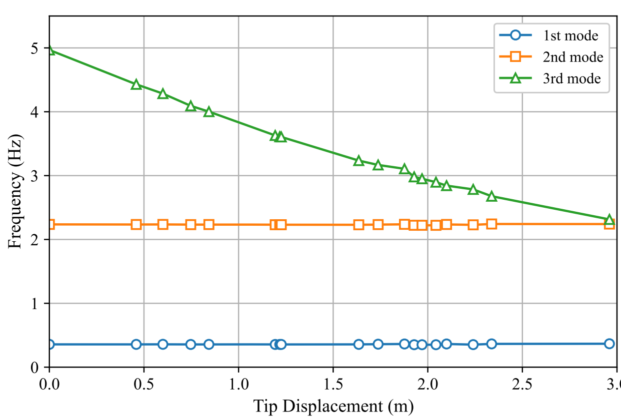

Fig. 10. Variation of frequencies with wing tip displacement magnitude.

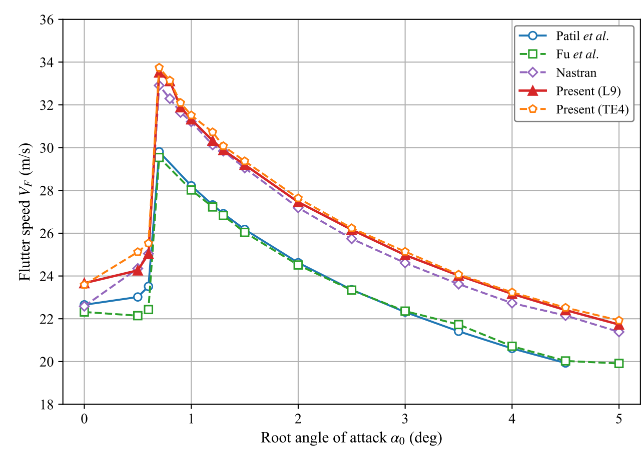

Fig. 11. Flutter speed vs. root angle of attack.

- The strip theory result agrees closely with Patil's reference value, confirming that the equivalent MSC.Nastran shell model accurately reproduces the structural dynamics of the HALE wing. The close match also validates the appropriateness of 2D Theodorsen aerodynamics for comparison with Peters' finite-state inflow model.
- Comparing the same MSC.Nastran structural model with different aerodynamic formulations shows that DLM predicts a 12.6% higher flutter speed than strip theory.
- The 1D CUF and MSC.Nastran shell models with DLM aerodynamics show good agreement, with a 1.1% difference.

3.1.3. Nonlinear flutter analysis

The nonlinear flutter analysis follows the piecewise linearization strategy, as shown in Fig. 1. At each velocity, the static equilibrium is computed via VLM-CUF coupling, then modal analysis is performed at the equilibrium state using the tangent stiffness. DLM and p-k flutter analysis are then employed using the modes at the equilibrium state. In this section, first, a numerical example concerning the equilibrium state is shown at $V_\infty = 21.75$ m/s and $\alpha_0 = 5°$ with the wing tip displacement reaching 2.24 m, i.e., 14% of semi-span. Fig. 5 shows the convergence history, achieving tolerance 10^{-4} within several iterations. Fig. 6

Table 5
Effect of CUF kinematic theories on natural frequencies (Hz).

Model	DOF	1^{st} Bend.	2^{nd} Bend.	1^{st} Tors.	1^{st} In-plane bend.
Reference					
Patil [1]	–	0.357	2.238	4.942	5.049
Taylor and 20B4					
TE1	549	0.357	2.237	–	5.012
TE2	1098	0.357	2.237	5.051	5.012
TE3	1830	0.357	2.237	5.051	5.006
TE4	2745	0.357	2.236	5.021	5.006
Lagrange and 20B4					
4LE9	4941	0.357	2.236	5.004	5.006
8LE9	9333	0.357	2.236	4.974	5.006
12LE9	13,725	0.357	2.236	4.968	5.006
MSC.Nastran Shell					
60×8	9462	0.357	2.235	4.926	5.006

Table 6
Flutter convergence analysis, 24×10 aerodynamic panels.

Model	DOF	V_F (m/s)	f_F (Hz)
Effect of spanwise structural mesh			
5B4-12LE9	3600	37.02	3.64
10B4-12LE9	6975	36.79	3.62
15B4-12LE9	10,350	36.78	3.61
20B4-12LE9	13,725	36.76	3.61
Effect of LE cross-sectional theory			
20B4-4LE9	4941	37.03	3.64
20B4-8LE9	9333	36.83	3.62
20B4-12LE9	13,725	36.76	3.61
Effect of TE cross-sectional theory			
10B4-TE4	1395	36.30	3.68
Shell			
MSC.Nastran	9462	36.31	3.57

Table 7
Linear flutter results from different aerodynamic models.

Structural Model	Aerodynamic Model	V_F (m/s)	f_F (Hz)
Patil [1]	Peters 2D finite-state	32.21	3.60
MSC.Nastran	Strip theory	32.29	3.57
MSC.Nastran	DLM	36.31	3.57
CUF Beam (LE9)	DLM	36.76	3.61
CUF Beam (TE4)	DLM	36.30	3.68

Table 8
Comparison of linear and nonlinear flutter analysis results.

Analysis	Structural Model	Aero Model	α_0	V_F (m/s)	f_F (Hz)
Linear	Patil [1]	2D Peters	–	32.21	3.60
	MSC.Nastran	2D Strip	–	32.29	3.57
	MSC.Nastran	3D DLM	–	36.31	3.57
	CUF Beam (LE9)	3D DLM	–	36.76	3.61
	CUF Beam (TE4)	3D DLM	–	36.30	3.68
Nonlinear	Patil [1]	2D Peters	4.5°	19.93	2.60
	MSC.Nastran Iterative	3D DLM	4.5°	22.15	2.61
	CUF Iterative (LE9)	3D DLM	4.5°	22.41	2.72
	CUF Iterative (TE4)	3D DLM	4.5°	22.52	2.72

presents the first three modes at the equilibrium state. To quantitatively assess the variations in modal shapes, the Modal Assurance Criterion (MAC) [39] is employed. The first comparison is between the baseline modes from the free-vibration analyses, and those at $V_\infty = 17.31$ m/s and $\alpha_0 = 5°$, as shown in Fig. 7. The second comparison is between the baseline modes from the free-vibration analyses, and those at $V_\infty = 21.75$ m/s and $\alpha_0 = 5°$, as shown in Fig. 8. The last comparison is between modes at $V_\infty = 17.31$ m/s and at $V_\infty = 21.75$ m/s, see Fig. 9.

Table 8 summarizes the flutter results, including both linear and nonlinear analyses with different aerodynamic models. Fig. 10 plots the first three frequencies as functions of wing tip displacement magnitude. The results show that:

- The frequencies from the nonlinear analysis are systematically lower than those from the linear one. While the first and second bending mode frequencies remain relatively constant across all displacement levels, the third mode exhibits pronounced frequency reductions.
- The linear analysis overestimates the flutter speed by more than 40% for this configuration.
- Mode shapes variations with respect to the linear case increase as the velocity grows.
- The CUF nonlinear result shows reasonable agreement with Patil's reference, with the difference attributable to the aerodynamic effects captured by DLM.

3.1.4. *Effect of root angle of attack*

Following the methodology of Patil et al. [1], flutter analyses are performed at α_0 values from 0 to 5 degrees, with the trim velocity iteratively matched to the flutter speed at each condition. Fig. 11 presents the flutter speed variation with root angle of attack. Figs. 12 and 13 present the flutter frequency and tip displacement variation with angle of attack. Table 9 provides a quantitative comparison of flutter results at selected angles of attack.

The displacement effect on flutter is further analyzed following Patil et al. [1]. The flutter boundary is obtained by relating flutter speed to wing-tip displacement and comparing that relation with trim-velocity–displacement curves at fixed root angle of attack. Fig. 14 shows that both flutter speed and flutter frequency decrease as the absolute wing-tip displacement increases.

Fig. 15 presents the trim velocity and wing-tip displacement for selected root angles of attack. As in Patil et al. [1], the intersections with the flutter-speed curve identify the trim states for which the equilibrium velocity and the flutter velocity are matched. Fig. 16 shows the corresponding damping and frequency branches. The results show that:

- At low angles, insufficient lift results in downward bending and flutter speeds of 22–25 m/s. A discontinuity at $\alpha_0 \approx 0.65°$ marks the transition from gravity-dominated to lift-dominated deformation, with flutter speed jumping to 30–34 m/s. This discontinuity corresponds to the structural transition from a gravity-dominated 'sagging' shape to a lift-dominated 'hogging' shape. The flutter speed decreases monotonically (32 to 22 m/s) due to increased geometric softening from larger deformations.
- The tip displacement transitions from −18% ($\alpha_0 = 0°$) to +14% ($\alpha_0 = 5°$) of semi-span. The strong correlation between tip displacement and flutter speed suggests that deformation monitoring could serve as an in-flight flutter margin indicator [1].
- The systematic 2–13% discrepancy between the present results and Patil's predictions arises from the different aerodynamics models adopted. This is quantitatively consistent with the linear flutter results (36.76 vs. 32.21 m/s, 14% difference).

3.2. *NACA 2415 wing*

To further assess the applicability of the proposed framework to realistic wing configurations, a NACA 2415 airfoil wing is considered. Varello et al. [24] analyzed the linear behavior of a straight aluminum wing with this airfoil profile, subjected to VLM aerodynamic loading at $\alpha = 3°$. The cross-section consists of an aluminum skin reinforced by front and rear spars at 25% and 75% chord, as shown in Fig. 17. The root section is clamped. Table 10 summarizes the model properties.

To validate the present VLM-CUF coupling on this configuration, the same case is reproduced using 20 B4 beam elements with LE9

Table 9
Flutter speed comparison at selected angles of attack.

α_0 (deg)	Patil [1] (m/s)	LE9 (m/s)	TE4 (m/s)	Diff. LE9–Patil (%)	LE9 f_F (Hz)
0.0	22.65	23.67	23.59	+4.50	2.17
0.5	23.02	24.26	25.12	+5.40	2.50
1.0	28.22	31.33	31.52	+11.0	3.33
2.0	24.62	27.46	27.64	+11.5	3.07
3.0	22.31	24.98	25.14	+12.0	2.88
4.5	19.93	22.41	22.52	+12.4	2.72

Table 10
NACA 2415 wing properties.

Property	Value	Unit
Semi-span (L, linear case)	5	m
Semi-span (L, nonlinear case)	16	m
Chord (c)	1	m
Front spar thickness (t_1)	0.015c	–
Rear spar thickness (t_2)	0.0105c	–
Skin thickness (t_3)	0.006c	–
Young's modulus (E)	69.0	GPa
Poisson's ratio (ν)	0.33	–
Density (ρ)	2700	kg/m^3
Air density (ρ_∞)	1.225	kg/m^3

Table 11
NACA 2415 wing ($b = 5$ m, $\alpha = 3°$, $V_\infty = 50$ m/s): static aeroelastic tip displacement u_z (mm).

Model	Spanwise mesh	u_z (mm)	Diff. vs. solid (%)
Varello TE3	20 B4	8.6485	−0.32
Varello TE4	20 B4	8.6723	−0.04
Varello solid model, SOL101	–	8.6762	0.00
Present LE9	20 B4	8.7280	+0.60

Table 12
NACA 2415 wing natural frequencies (Hz) and linear flutter speed (m/s).

Model	1st Bend.	In-plane	1st Tors.	V_F
Present (LE9)	0.585	3.132	15.93	197.8

Table 13
NACA 2415 wing: nonlinear flutter analysis results.

α_0 (deg)	V_F (m/s)	f_F (Hz)	Tip/Semi-span (%)
0	199.52	7.53	−7.01
0.5	170.03	2.80	17.35
1	154.06	2.61	22.93
2	140.40	2.34	30.47
3	134.96	2.17	35.98
5	126.26	1.95	42.49
7	121.09	1.83	46.81

cross-sectional expansion. Table 11 compares the tip displacement u_z at $\alpha = 3°$, $V_\infty = 50$ m/s with four models. The present VLM-based results agree with the reference. Having validated the framework on the original Varello configuration, the semi-span is extended to 16 m, identical to the HALE case, to promote large deformations and enable the investigation of geometric nonlinear effects. The original 5 m wing exhibits negligible geometric nonlinearity due to its high stiffness-to-load ratio, whereas the extended 16 m configuration produces tip deflections exceeding 40% of the semi-span. Table 12 reports the natural frequencies and flutter velocity. Nonlinear flutter analyses are performed at root angles of attack from 0° to 7°, see Table 13. Figs. 18–20 present the flutter speed, flutter frequency, and tip displacement variations with root angle of attack. A significant change in the flutter mechanism is observed: the linear case exhibits classical bending-torsion flutter, whereas under geometric nonlinearity the in-plane bending mode acquires significant torsional character through geometric coupling induced by the large bending curvature, resulting in flutter at a substantially lower frequency.

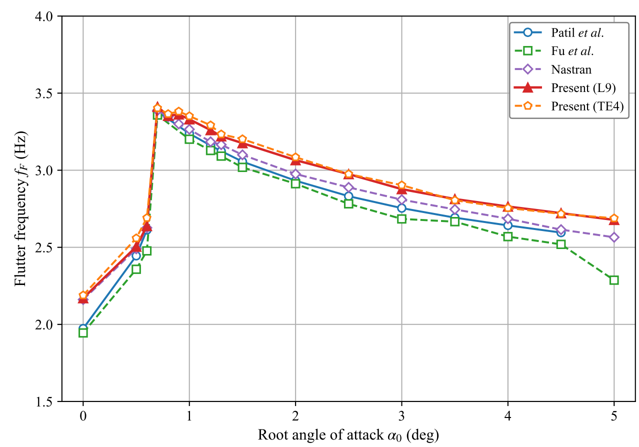

Fig. 12. Flutter frequency vs. root angle of attack.

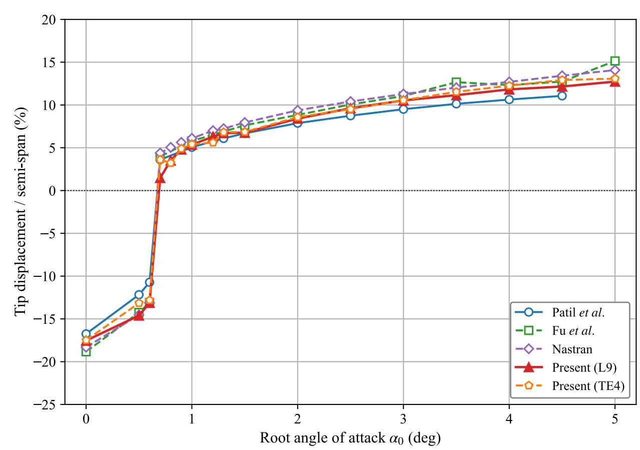

Fig. 13. Wing tip displacement vs. root angle of attack.

3.3. Discussion

Tables 2–5 show that the bending frequencies change little across the structural models, whereas the first torsional frequency is more sensitive to the cross-sectional expansion. TE1 does not identify this torsional mode, while the higher-order TE and LE models converge to similar frequencies. Representing torsional deformation therefore requires richer cross-sectional kinematics. Once the structural frequencies are matched, the CUF and shell models with DLM aerodynamics predict nearly the same flutter boundary. The lower flutter speed obtained with strip theory reflects the aerodynamic representation rather than differences in structural modal characteristics.

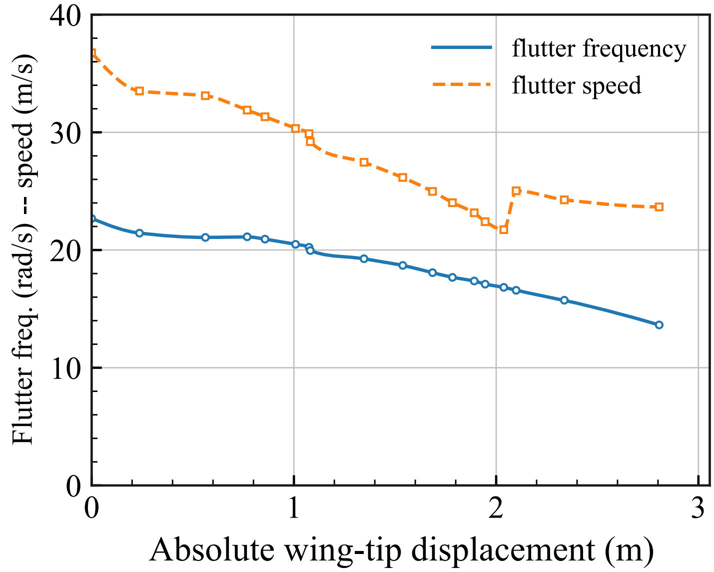

Fig. 14. Variation of flutter speed and flutter frequency with wing-tip displacement for the CUF LE9 HALE model.

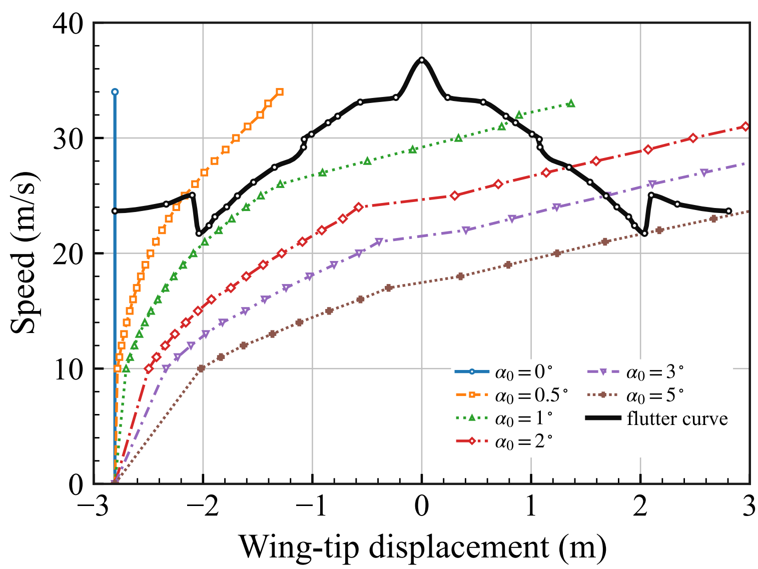

Fig. 15. Correlation of flutter speed, trim velocity, and wing-tip displacement for selected root angles of attack.

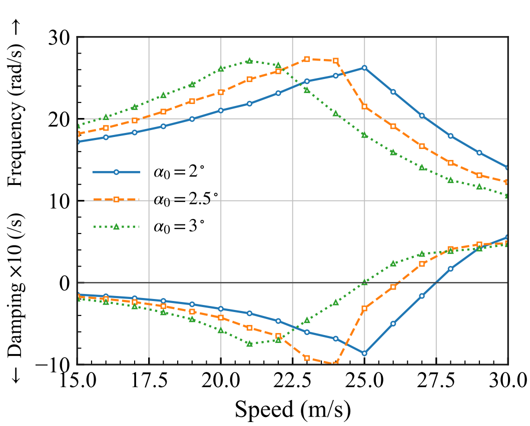

Fig. 16. Flutter damping and frequency branches for selected root angles of attack.

At a nonlinear equilibrium, the static deformation changes the tangent stiffness and, consequently, the modal properties used in the flutter analysis. Fig. 10 shows that the first two bending frequencies remain nearly constant as the wing-tip displacement increases, whereas the first torsional frequency decreases markedly. The deformed-configuration modes also develop coupling between in-plane bending and torsion. This coupling arises from the deformed equilibrium and is absent in the linear modes. The reduction in the first torsional frequency changes the structural dynamics entering the flutter calculation and contributes to the decrease in flutter speed and flutter frequency.

For both the HALE and NACA 2415 wings, root angle of attack affects the flutter boundary through the corresponding equilibrium deformation. Gravity produces downward bending at low lift, while increasing aerodynamic load changes the displacement's sign and magnitude. In the HALE case, the transition between gravity-dominated and lift-dominated equilibria produces the discontinuity at low angle of attack. Beyond this transition, and over the higher-angle NACA 2415 cases, larger equilibrium deformation is accompanied by lower flutter speed

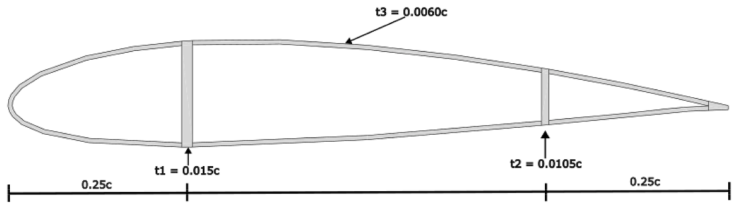

Fig. 17. NACA 2415 three-cell cross-section with front and rear spars at 25% and 75% chord.

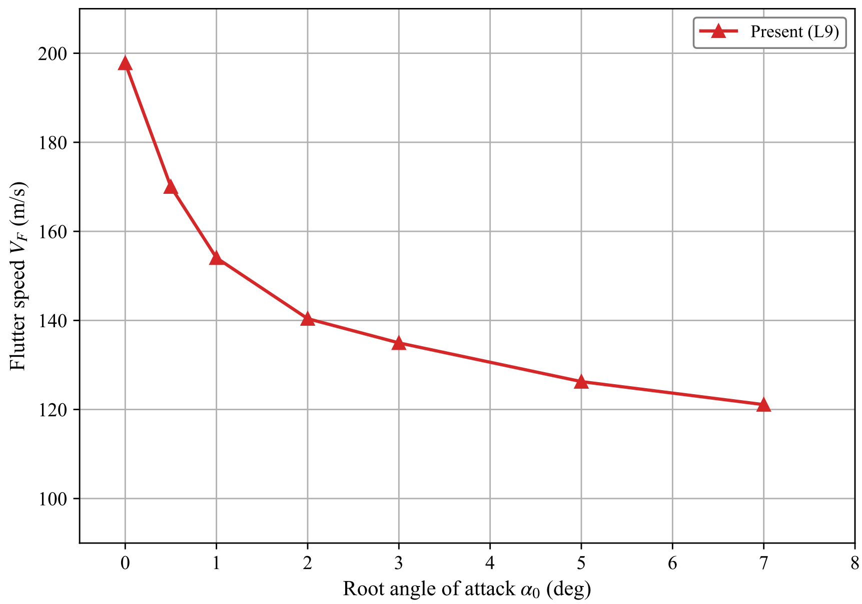

Fig. 18. NACA 2415 wing flutter speed vs. root angle of attack.

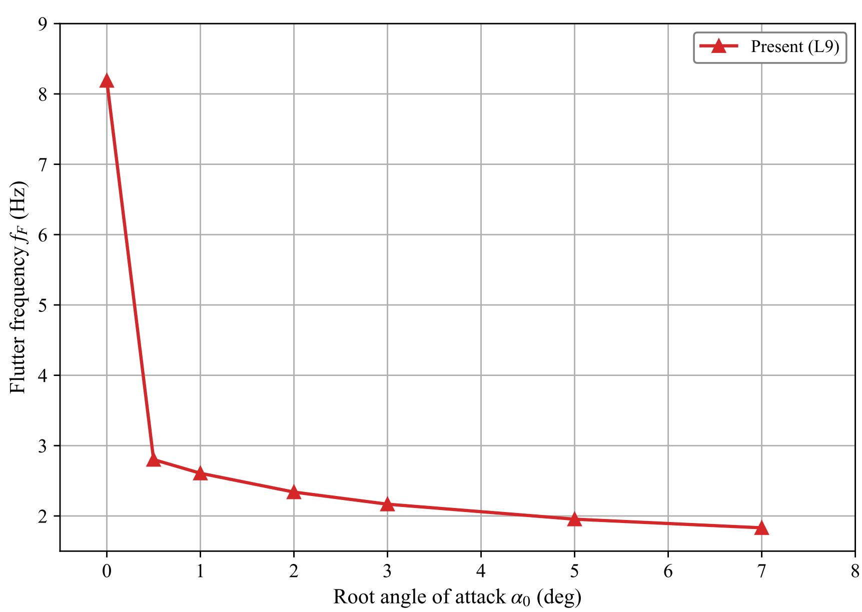

Fig. 19. NACA 2415 wing flutter frequency vs. root angle of attack.

and frequency. This trend agrees with previous nonlinear aeroelastic studies of highly flexible wings [1,3,4].

The advantages of the present formulation, compared with models in the literature and commercial codes, stem from a reduced number of DOF and the ability to tune the structural-theory kinematics to detect aeroelastic phenomena. In particular, adding higher-order torsion terms is critical to improving the 1D model's accuracy. This significantly reduces the overall unknowns, as only one-third of the shell model's DOF are required. The choice of the structural theory can be made through a convergence analysis on the expansion order. In most cases, for conventional wing architectures, third-order expansions provide sufficiently accurate results.

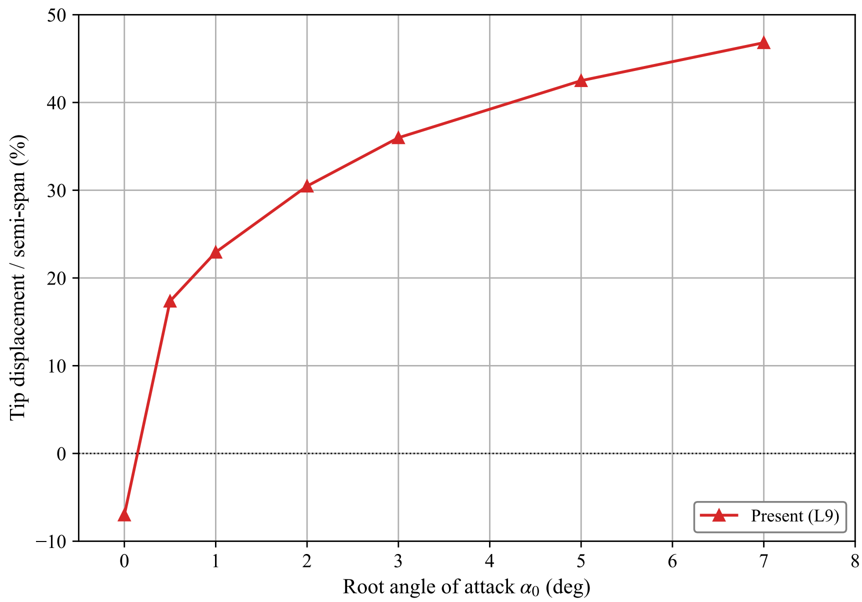

Fig. 20. NACA 2415 wing tip displacement vs. root angle of attack.

4. Conclusions

Nonlinear aeroelastic analyses of highly flexible wings have been presented in this paper. 1D CUF beam models were coupled with VLM for steady aerodynamic loads and with a DLM for unsteady aerodynamics. A piecewise linearization strategy was employed to evaluate the flutter boundary about the statically deformed equilibrium. At each prescribed velocity, modal analysis is performed and the aerodynamic mesh is updated at the same converged equilibrium before the trim and predicted flutter velocities are matched. The framework was validated against literature results and MSC.Nastran shell-based models. Furthermore, a wing with a NACA airfoil was analyzed. The analyses conducted indicate the following:

- CUF models achieve natural frequency and linear flutter predictions within 1% of MSC.Nastran shell references. The DLM aerodynamics predicts 10–15% higher flutter speeds than 2D strip theory.
- Geometric nonlinearity reduces the HALE wing flutter speed by up to 39% at $\alpha_0 = 4.5°$ and modifies modal shapes with coupling between in-plane bending and torsion.
- A parametric study over root angle of attack reveals a strong correlation between wing tip displacement and flutter speed. The nonlinear flutter speed decreases monotonically with increasing $\alpha_0 > 1°$, consistent with the literature.
- Application to the NACA 2415 wing demonstrates that the framework is applicable to realistic thin-walled configurations. A 39% reduction in flutter speed is observed, with a change in flutter mechanism from classical bending-torsion coalescence to geometric-coupling-induced instability at lower frequencies.

The proposed framework provides a computationally efficient tool for the preliminary nonlinear aeroelastic design of flexible aircraft. Further extensions should consider some of the assumptions or limitations of the present work. The piecewise linearization procedure evaluates linearized stability about nonlinear static equilibrium states and does not describe post-flutter limit-cycle oscillations or fully nonlinear time-domain aeroelastic response. VLM and DLM are based on attached, inviscid, subsonic potential flow and therefore do not account for separated flow or stall. Future work will include experimental validation, time-domain nonlinear aeroelastic simulations, and laminated composite wings.

CRediT authorship contribution statement

Zhuolin Ying: Writing – original draft, Validation, Conceptualization; **Rodolfo Azzara:** Writing – review & editing, Supervision, Methodology, Conceptualization; **Matteo Filippi:** Writing – review & editing, Supervision, Methodology, Conceptualization; **Ma Xiaoping:** Writing – review & editing, Supervision, Funding acquisition; **Marco Petrolo:** Writing – review & editing, Supervision, Methodology, Conceptualization.

Declaration of competing interest

The authors declare that they have no known competing financial interests or personal relationships that could have appeared to influence the work reported in this paper.

Data availability

Data will be made available on request.

References

[1] M.J. Patil, D.H. Hodges, C.E.S. Cesnik, Nonlinear aeroelasticity and flight dynamics of high-altitude long-endurance aircraft, J. Aircr. 38 (1) (2001) 88–94.
[2] T.E. Noll, J.M. Brown, M.E. Perez-Davis, S.D. Ishmael, G.C. Tiffany, M. Gaier, Investigation of the Helios Prototype Aircraft Mishap, Technical Report NASA/TM-2004-212953, NASA, 2004.
[3] D.M. Tang, E.H. Dowell, Effects of geometric structural nonlinearity on flutter and limit cycle oscillations of high-aspect-ratio wings, J. Fluid. Struct. 19 (3) (2004) 291–306.
[4] M.J. Patil, D.H. Hodges, On the importance of aerodynamic and structural geometrical nonlinearities in aeroelastic behavior of high-aspect-ratio wings, J. Fluid. Struct. 19 (7) (2004) 905–915.
[5] D.H. Hodges, Geometrically exact, intrinsic theory for dynamics of curved and twisted anisotropic beams, AIAA J. 41 (6) (2003) 1131–1137.
[6] C.E.S. Cesnik, E.L. Brown, Modeling of high aspect ratio active flexible wings for roll control, in: 43rd AIAA/ASME/ASCE/AHS/ASC Structures, Structural Dynamics, and Materials Conference, 2002, pp. AIAA Paper 2002–1719.
[7] W. Su, C.E.S. Cesnik, Strain-based analysis for geometrically nonlinear beams: a modal approach, J. Aircr. 51 (3) (2014) 890–903.
[8] R. Palacios, J. Murua, R. Cook, Structural and aerodynamic models in nonlinear flight dynamics of very flexible aircraft, AIAA J. 48 (11) (2010) 2648–2659.
[9] D.A. Peters, S. Karunamoorthy, W.M. Cao, Finite state induced flow models – Part I: two-dimensional thin airfoil, J. Aircr. 32 (2) (1995) 313–322.
[10] E. Albano, W.P. Rodden, A doublet-lattice method for calculating lift distributions on oscillating surfaces in subsonic flows, AIAA J. 7 (2) (1969) 279–285.

[11] O. Avin, D.E. Raveh, A. Drachinsky, Y. Ben-Shmuel, M. Tur, Experimental aeroelastic benchmark of a very flexible wing, AIAA J. 60 (3) (2022) 1745–1768.
[12] M. Ritter, J. Hilger, A. Ribeiro, A.E. Öngüt, M. Righi, D.E. Raveh, et al., Collaborative Pazy wing analyses for the third aeroelastic prediction workshop, in: AIAA SciTech Forum, Orlando, FL, 2024.
[13] J.P.T.P. Santos, F.D. Marques, G.R. Begnini, Influence of nonlinear static deformation on the pre-Pazy and Pazy wing flutter, J. Aircr. (2025).
[14] C. Riso, C.E.S. Cesnik, Impact of low-order modeling on aeroelastic predictions for very flexible wings, J. Aircr. 60 (3) (2023) 662–687.
[15] K.C.W. Cheng, A. Cea, R. Palacios, A. Castrichini, T. Wilson, Nonlinear gust effects on flexible aircraft with flared hinged wings, in: International Forum on Aeroelasticity and Structural Dynamics (IFASD), The Hague, Netherlands, 2024.
[16] L. Euler, De curvis elasticis. Methodus Inveniendi Lineas Curvas Maximi Minimive Proprietate Gaudentes, Sive Solutio Problematis Isoperimetrici Lattissimo Sensu Accepti, Bousquet, 1744.
[17] D. Bernoulli, De vibrationibus et sono laminarum elasticarum, Comment. Acad. Sci. Imp. Petropolitanae (1751).
[18] S.P. Timoshenko, On the correction for shear of the differential equation for transverse vibrations of prismatic bars, Philos. Mag. 41 (1921) 744–746.
[19] E. Carrera, M. Cinefra, M. Petrolo, E. Zappino, Finite Element Analysis of Structures Through Unified Formulation, John Wiley & Sons, Chichester, UK, 2014.
[20] E. Carrera, G. Giunta, M. Petrolo, Beam Structures: Classical and Advanced Theories, John Wiley & Sons, Chichester, UK, 2011.
[21] E. Carrera, M. Petrolo, E. Zappino, Performance of CUF approach to analyze the structural behavior of slender bodies, J. Struct. Eng. 138 (2) (2012) 285–297.
[22] M. Petrolo, E. Zappino, E. Carrera, Refined free vibration analysis of one-dimensional structures with compact and bridge-like cross-sections, Thin-Wall. Struct. 56 (2012) 49–61.
[23] D. Scano, E. Carrera, M. Petrolo, Use of the 3D equilibrium equations in the free-edge analyses for laminated structures with the variable kinematics approach, Aerotec. Missili Spaz. 103 (2024) 179–195.
[24] A. Varello, E. Carrera, L. Demasi, Vortex lattice method coupled with advanced one-dimensional structural models, J. Aeroelast. Struct. Dyn. 2 (2) (2011) 53–78.
[25] M. Petrolo, Flutter analysis of composite lifting surfaces by the 1D Carrera Unified Formulation and the doublet lattice method, Compos. Struct. 95 (2013) 539–546.
[26] M. Petrolo, Advanced 1D structural models for flutter analysis of lifting surfaces, Int. J. Aeronaut. Space Sci. 13 (2) (2012) 199–209.
[27] A. Pagani, M. Petrolo, E. Carrera, Flutter analysis by refined 1D dynamic stiffness elements and doublet lattice method, Adv. Aircr. Spacecr. Sci. 1 (3) (2014) 291–310.
[28] C.R. Vindigni, G. Mantegna, A. Esposito, C. Orlando, A. Alaimo, An aeroelastic beam finite element for time domain preliminary aeroelastic analysis, Mech. Adv. Mater. Struct. 30 (5) (2023) 1064–1072.
[29] C.R. Vindigni, G. Mantegna, C. Orlando, A. Alaimo, M. Berci, A refined aeroelastic beam finite element for the stability analysis of flexible subsonic wings, Comput. Struct. 307 (2025) 107618.
[30] S.A. Jalalian, H. Tourajizadeh, S.A.A. Hosseini, Modelling and nonlinear control of aircraft wings flutter by use of piezoelectric patch considering the airfoil shape cross section of the wing beam, Nonlinear Dyn. 113 (19) (2025) 25429–25458.
[31] V. Gulizzi, I. Benedetti, Computational aeroelastic analysis of wings based on the structural discontinuous Galerkin and aerodynamic vortex lattice methods, Aerosp. Sci. Technol. 144 (2024) 108808.
[32] M. Grifò, A. Da Ronch, I. Benedetti, A computational aeroelastic framework based on high-order structural models and high-fidelity aerodynamics, Aerosp. Sci. Technol. 132 (2023) 108069.
[33] R. Azzara, M. Filippi, M. Petrolo, R. Ricci, G. Zecchin, Improved aeroelastic analysis framework to assess shear and cross-section deformability effects on static aeroelastic response, Proc. Inst. Mech. Eng. G: J. Aerosp. Eng. 240 (11)(2026) 1648–1667.
[34] R.L. Harder, R.N. Desmarais, Interpolation using surface splines, J. Aircr. 9 (2) (1972) 189–191.
[35] J. Katz, A. Plotkin, Low-Speed Aerodynamics, Cambridge University Press, Cambridge, UK, 2nd ed., 2001.
[36] W.P. Rodden, P.F. Taylor, S.C. McIntosh, Further refinement of the subsonic doublet-lattice method, J. Aircr. 35 (5) (1998) 720–727.
[37] L. Demasi, Introduction to Unsteady Aerodynamics and Dynamic Aeroelasticity, Springer Cham, 2024.
[38] H.J. Hassig, An approximate true damping solution of the flutter equation by determinant iteration, J. Aircr. 8 (11) (1971) 885–889.
[39] R.J. Allemang, The modal assurance criterion – twenty years of use and abuse, Sound Vib. 37 (8) (2003) 14–23.